Co-published by
Institute of Fluid-Flow Machinery
Polish Academy of Sciences
Committee on Thermodynamics and Combustion
Polish Academy of Sciences

http://www.imp.gda.pl/archives-of-thermodynamics/

ARCHIVES OF THERMODYNAMICS

Delineating the influence of solvent fraction and temperature-dependent heat source/sink on magneto-convective flow: A response surface methodology and an artificial neural network approach

S.K. Abhilasha[a*], Manoranjan Parhi[b], Harjot Singh Gill[c], Nagaraj Patil[d], M. Umeshaiah[e]

[a]Department of Studies in Mathematics, Davangere University, Davangere 577007, Karnataka, India
[b]Department of Computer Science and Engineering, Siksha 'O' Anusandhan (Deemed to be University), Bhubaneswar, Odisha 751030, India
[c]Department of Mechanical Engineering, Chandigarh University, Mohali 140307, Punjab, India
[d]Department of Mechanical Engineering, School of Engineering and Technology, JAIN (Deemed to be University), Bangalore 562112, Karnataka, India
[e]Department of Mathematics, PES Institute of Technology & Management, Shivamogga 577204, Karnataka, India
*Corresponding author email: abhilashaskmaths@gmail.com

Received: 26.08.2025; revised: 02.03.2026; accepted: 04.03.2026

Abstract

The present study investigates the influence of a non-uniform heat sink/source on the unsteady flow of Boger liquid via a slowly rotating stretching disk subjected to suction and convective boundary conditions. This study is significant because it helps optimise cooling and heating processes in chemical, pharmaceutical and energy systems. The research also highlights methods for managing heat and mass transport in porous and industrial materials. Overall, it helps to improve performance, stability and energy efficiency in engineering and applied science. Dimensionless ordinary differential equations are obtained by transforming the governing partial differential equations using similarity variables. The resultant non-dimensional ordinary differential equations are solved numerically utilising the finite difference method. Furthermore, the fluid flow, mass and heat transfer and are evaluated using an artificial neural network approach. Additionally, the response surface methodology is used to assess the heat transmission rate statistically. The influence of different parameters on the concentration, velocity and thermal profiles is exemplified graphically. Increasing the suction parameter, relaxation time ratio and magnetic parameter reduces the velocity profile. The thermal profile enhances as the space and temperature-dependent heat sink/source parameters increase.

Keywords: Boger fluid; Non-uniform heat source/sink; Activation energy; Convective boundary conditions; Slow rotating disk

Vol. 47(2026), No. 2, 69–85; doi: 10.24425/ather.2026.158675

Cite this manuscript as: Abhilasha, S.K, Parhi, M., Gill, H.S., Patil, N., & Umeshaiah, M. (2026). Delineating the influence of solvent fraction and temperature-dependent heat source/sink on magneto-convective flow: A response surface methodology and an artificial neural network approach. *Archives of Thermodynamics*. 47(2), 69–85.

1. Introduction

Heat transfer (HT) is a crucial and extensively used discipline within engineering. Additionally, a lot of research has been done on increasing the rate of HT, which is important for many applications, including storing radioactive nuclear waste, cooling electronic components, catalysts, heat exchangers, and more. Enhancing the rate of HT can be achieved by using several liquid types, particularly nanoliquid and hybrid nanoliquid, which are created by combining one or more types of highly thermally conductive nanoparticles. The function of liquids in the process of HT has been discussed in several significant scientific publications. Recently, Chamkha and Pop [1] examined the HT characteristics of a laminar boundary layer flow of a viscous liquid past a vertical plate. Kattimani et al. [2] used a Levenberg-Marquardt artificial neural network (ANN) to investigate HT behaviour at the stagnation-point motion of a fluid past an off-centred disk. Kumar et al. [3] elucidated the HT characteristics of hybrid

Nomenclature

A – constant, $A = -w_0/2\sqrt{\frac{\nu_f \Omega_0}{1-\alpha t}}$

A^*, B^* – space and temperature-dependent heat source/sink parameters

B_0 – magnetic field, $\sqrt{\frac{\text{kg}\Omega}{\text{s}}}\,\text{m}^{-1}$

Bi – Biot number, $\text{Bi} = \frac{h_f}{k_f}\sqrt{\frac{\nu_f(1-\alpha t)}{\Omega_0}}$

c – stretching rate, s^{-1}

C – concentration

C_p – specific heat, J $\text{kg}^{-1}\,\text{K}^{-1}$

D_B – diffusion coefficient, $\text{m}^2\,\text{s}^{-1}$

E – dimensionless activation energy, $E = E_a/KT_\infty$

E_a – activation energy, kg $\text{m}^2\,\text{s}^{-2}$

(F, G, H) – velocity profiles

h_f – heat transfer coefficient, W $\text{m}^{-2}\text{K}^{-1}$

k_f – thermal conductivity, W $\text{m}^{-1}\,\text{K}^{-1}$

k_r^2 – reaction rate, s^{-1}

K – Boltzmann constant, kg $\text{m}^2\,\text{s}^{-2}\,\text{K}^{-1}$

M – magnetic parameter, $M = \sigma_f B_0^2/\rho_f \Omega_0$

p – pressure, kg $\text{m}^{-1}\,\text{s}^{-2}$

P – dimensionless pressure

Pr – Prandtl number, $\text{Pr} = (\mu C_p)_f/k_f$

q''' – non-uniform heat source/sink coefficient, W m^{-3}

r, z – coordinates, m

Re – Reynolds number,

Sc – Schmidt number, $\text{Sc} = \nu_f/D_B$,

t – time, s

T – temperature, K

T_∞ – ambient temperature, K

T_w – surface temperature, K

(u, v, w) – velocity components, m s^{-1}

w_0 – suction velocity, m s^{-1}

Greek symbols

α – angular velocity, s^{-1}

α^* – dimensionless quantity, $\alpha^* = \alpha/\Omega_0$

β_1 – solvent fraction parameter

β_2 – ratio of relaxation time

δ – temperature-difference parameter, $\delta = (T_w - T_\infty)/T_\infty$

γ_1 – stretching ratio parameter, $\gamma_1 = c/\Omega_0$

$\theta(\eta)$ – thermal profile

μ_f – dynamic viscosity, kg $\text{m}^{-1}\,\text{s}^{-1}$

ν_f – kinematic viscosity, $\text{m}^2\,\text{s}^{-1}$

ρ_f – density, kg m^{-3}

σ_f – electrical conductivity, $\Omega^{-1}\,\text{m}^{-1}$

σ^* – chemical reaction rate parameter, $\sigma^* = k_r^2(1-\alpha t)/\Omega_0$

$\phi(\eta)$ – concentration profile

Ω_0 – positive constant, s^{-1}

Subscripts and Superscripts

∞ – ambient

f – fluid

w – wall

Abbreviations and Acronyms

AE – activation energy

ANN – artificial neural network

C-BC – convective boundary condition

DE – differential equation

FDM – finite difference method

HT – heat transfer

MF – magnetic field

MHD – magnetohydrodynamics

N-HSS – non-uniform heat source/sink

ODE – ordinary differential equation

PDE – partial differential equation

RSM – response surface methodology

nanoliquid motion through a stretchy cylinder. Hussain et al. [4] studied HT variations of the Casson ternary nanoliquid motion using ANN. Eegunjobi et al. [5] investigated HT features of an electrically conducting liquid flow via an expanding surface.

Boger liquids are the elastic liquids with a constant viscosity irrespective of shear rate, which allows them to differentiate between elastic and viscous effects in viscoelastic flows. Their flexibility enables progress in materials science, agriculture, gas and oil. These liquids are also very important for consumer products like cosmetics and food, where controlling viscosity is essential. These liquids are created by mixing a small quantity of polymer with a high-viscosity Newtonian liquid. This makes a substance that has properties of both a liquid and a solid. In order to overcome the shear thinning caused by the polymer additions, highly viscous solvents are used to form Boger liquids. When exploring elastic characteristics without the restriction of shear thinning, these fluids are essential. Norouzi et al. [6] elucidated the pressure drop of a Boger liquid motion at the inertia regime. Banakar et al. [7] examined the motion of Boger liquid over a rotating rough disk with a solid-liquid interfacial layer impact. Veeranna et al. [8] deliberated the Boger micropolar liquid flow across a semi-circular body. The experimental comparison of the interfacial wave behaviour of the Boger liquid stream in microchannels was explained by Hue et al. [9].

Under the influence of an external magnetic field (MF), investigators have conducted both experimental and theoretical studies on the thermomagnetic circulation of magnetic liquids that contain various geometries. Understanding the connection between an MF and the characteristics of a liquid flow has been a major focus in the study of electrically conducting fluid motion for many years. Further, magnetohydrodynamics (MHD) deliberates the behaviour of electrically conductive liquids in the presence of MFs. When subjected to an external MF, it exhibits distinctive behaviours such as magneto-viscous, magneto-optical and magneto-thermal impacts. Srihari et al. [10] scrutinised the Casson liquid flow in a vertical microchannel with the MF effect. Krishna et al. [11] deliberated the motion of a second-grade liquid with the effect of MF past a permeable surface. Preethi et al. [12] inspected the outcome of MF and thermal radiation on the flow of nanoliquid via an extended sheet. Takhar et al. [13] addressed the unsteady HT in the presence of MF on a semi-infinite plate. Takhar et al. [14] studied the HT behaviour on the unsteady MHD liquid motion influenced by MF over a stretchy surface. Jagadha et al. [15] exemplified the impact of MF on the MHD Casson liquid flow along an extending surface.

Non-uniform heat source/sinks (N-HSSs) are unevenly distributed, with changing amounts added or removed from a liquid across a specific area. Since these situations can change the flow properties of the liquid system and HT, they are important to many industrial applications. Temperature control is essential in the manufacture of chemicals and polymers since configurations can significantly impact the convective HT rates. Non-uniform heat sources placed into fluid flow can cause deviations in the flow's pressure, thermal and velocity profiles. Kumar et al. [16] elucidated the N-HSS influence on the time-varying nanoliquid motion past a permeable slider. Banakar et al. [17] inspected the outcome of N-HSS impacts on the bioconvective liquid flow between two parallel disks. Thumma et al. [18] investigated the influence of N-HSS on the Maxwell nanoliquid flow over a stretchy sheet. Banakar et al. [19] examined the impact of N-HSS on the tetra hybrid nanliquid motion past a rotating rough disk with the Levenberg-Marquardt ANN. Algehyne et al. [20] discovered the HT features of the MHD flow of micropolar liquid with the influence of N-HSS across a stretchable surface.

In 1889, Svante Arrhenius developed the idea of activation energy (AE), referring to the smallest energy required for potential reactants in a chemical system to undergo a reaction. A reaction takes place when atoms move rapidly due to this AE. This concept is vital in chemistry and is prevalent in many chemically reactive systems, such as oil reservoirs, food processing, geothermal systems and chemical engineering. Mass transfer is inevitable in the mixture whenever a concentration difference exists between two species during a chemical reaction. As a result, the concentration will naturally move from the species with a greater concentration to one with a lesser concentration. Salahuddin et al. [21] exemplified the AE consequence on the Casson liquid flow past an exponential surface. Hayat et al. [22] deliberated the significance of AE on third-grade hydromagnetic nanofluid flow past an elongating sheet. Asjad et al. [23] probed the Williamson liquid motion under the effect of AE and bioconvection. Samantha and Mondal [24] inspected the consequence of AE on the nanoliquid flow via a stretching disk. Srilatha et al. [25] delved into the effect of AE on the chemically reactive liquid motion past a stretching disk.

Defining convective boundary conditions (C-BCs) is important for understanding how heat moves between a fluid and a solid surface. This is especially relevant in studies of cooling systems and heat exchangers, where temperature differences are significant near the solid boundaries. These types of boundary conditions are commonly applied in nuclear power plants, gas turbines and thermal energy storage. C-BCs are typically used to analyse the temperature in order to produce a linear heat exchange for some algebraic values. Akbar et al. [26] deliberated the MHD liquid flow with the radiation influence via an elongating sheet using C-BC. By employing C-BC, Malik et al. [27] exemplified the outcome of C-BC on the Sisko liquid motion over an elongating surface. Shaw et al. [28] assessed the effects of C-BC and thermal convection on the Casson nanoliquid over a horizontal plate. The C-BC outcome on the Maxwell nanoliquid flow via a stretchy surface was addressed by Wang et al. [29]. The incompressible flow of nanoliquid in the occurrence of C-BC and variable thermal conductivity impacts across a surface was examined by Abbas and Khan [30].

Examining decelerating spinning disks is necessary for understanding a range of industrial applications where liquid mixing is essential, such as lubrication systems and stirred tanks. These disks are also used in brakes, flywheels and gas turbines, all of which are often employed in sectors such as analytical chemistry. A slow-rotating disk generally refers to a circular object that spins at a minimal rate of angular velocity. The interaction between the disk's rotation and the viscous fluid can create intricate flow patterns, influencing efficiency and performance. Rafiq et al. [31] probed the HT modelling with variable fluid characteristics on the unsteady revolving fluid motion across a rotating decelerated porous disk. They measured the degradation rate of the decelerated disk's angular velocity. Using a decelerating rotating disk, Ahmed et al. [32] assessed the thermal energy transfer in thin-film Buongiorno nanofluid flow with thermophoresis and Brownian motion. Ejaz and Mustafa [33] scrutinised the unsteady flow and compared different viscosity models across a slow-revolving disk with various physical properties. Lin et al. [34] observed the flow of nanoliquid via a spinning disk with surface temperature. Ali et al. [35] scrutinised the flow of the Sutterby fluid past a revolving disk with convection.

To the best of the author's knowledge, there has been no prior research on the unsteady Boger liquid motion past an expandable slowly rotating disk under the impact of N-HSS, AE and C-BC. This gap in previous studies forms the core research gap. In view of this, the current work scrutinised the consequences of AE and suction on the time-dependent motion of the Boger liquid over a slowly rotating stretched disk in the presence of N-HSS, chemical reactions, C-BCs and MF. The technical uses of slow-rotating disks involve flow in centrifugal filtering processes, food and chemical processing sectors, rotating machinery, and constructing multi-pore distributors. The combination of slow-rotating stretching disks with the AE impact provides a successful structure for examining the behaviour of reacting fluids under simultaneous mechanical and thermal influences. Further, analysing MF effects has substantial implications for chemistry, physics and engineering. The interface of electrically conductive fluids with MFs affects various industrial apparatus, such as bearings, pumps, MHD generators and boundary layer control systems. Similarity variables are used to convert the governing partial differential equations (PDEs) into dimensionless ordinary differential equations (ODEs). Additionally, the finite difference method (FDM) technique is utilised to numerically solve the derived ODEs, and the ANN approach is used to evaluate the fluid's mass, heat and flow transport profiles. Additionally, the response surface methodology (RSM) is utilised to address the HT rate of the liquid flow statically. Visual representations of the impact of various non-dimensional parameters on the concentration, temperature and velocity profiles are provided.

2. Mathematical formulation

Consider the unsteady flow of Boger fluid via a stretchy disk that rotates slowly, subjected to an MF $B(t)$. Let the velocity components be (u, v, w), and t denotes time, while p is the pressure. Figure 1 illustrates the flow geometry of the current model.

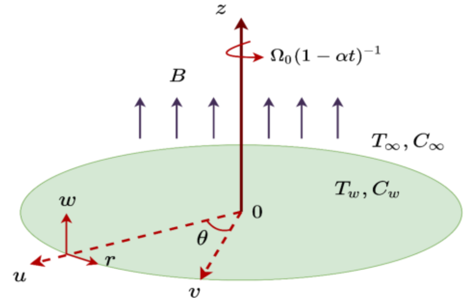

Fig. 1. Flow geometry.

The current modelling is predicated on the following assumptions:

- The main reason for the stream's instability is anticipated to be the disk's angular velocity.
- The disk's slowness is attributable to its angular velocity, which exhibits an opposite relationship with time.
- The effect induced by MF, $B(t)=\frac{B_0}{\sqrt{1-\alpha t}}$, is perpendicular to the surface of the disk and influences the fluid motion throughout the field.
- To analyse heat transmission behaviour, both C-BCs and N-HSS are considered.
- The consequences of AE and chemical reactions on the transfer of mass are taken into account.

Considering the assumptions above, the governing equations of the current model are expressed below (see [36−41]). Equations (1)–(6) represent the continuity, conservation of momentum, energy and concentration for the present flow problem.

$$\frac{\partial}{\partial r}(ur)+\frac{\partial}{\partial z}(wr)=0, \tag{1}$$

$$u\frac{\partial u}{\partial r}+\frac{\partial p}{\partial r}\frac{1}{\rho_f}+\frac{\partial u}{\partial t}-\frac{v^2}{r}+w\frac{\partial u}{\partial z}=\nu_f\left(\frac{1+\beta_1}{1+\beta_2}\right)\left[\frac{\partial^2 u}{\partial r^2}+\frac{\partial^2 u}{\partial z^2}+\frac{\partial}{\partial r}\left(\frac{u}{r}\right)\right]-\frac{\sigma_f u B(t)^2}{\rho_f}, \tag{2}$$

$$\frac{\partial v}{\partial t}+u\frac{\partial v}{\partial r}+\frac{uv}{r}+w\frac{\partial v}{\partial z}=\nu_f\left(\frac{1+\beta_1}{1+\beta_2}\right)\left[\frac{\partial^2 v}{\partial r^2}+\frac{\partial}{\partial r}\left(\frac{v}{r}\right)+\frac{\partial^2 v}{\partial z^2}\right]-\frac{\sigma_f v B(t)^2}{\rho_f}, \tag{3}$$

$$u\frac{\partial w}{\partial r}+\frac{\partial w}{\partial t}+w\frac{\partial w}{\partial z}=-\frac{\partial p}{\partial z}\frac{1}{\rho_f}+\nu_f\left(\frac{1+\beta_1}{1+\beta_2}\right)\left[\frac{\partial^2 w}{\partial z^2}+\frac{\partial^2 w}{\partial r^2}+r^{-1}\frac{\partial w}{\partial r}\right], \tag{4}$$

$$\frac{\partial T}{\partial t}+u\frac{\partial T}{\partial r}+w\frac{\partial T}{\partial z}=\frac{k_f}{(\rho C_p)_f}\left[r^{-1}\frac{\partial T}{\partial r}+\frac{\partial^2 T}{\partial z^2}+\frac{\partial^2 T}{\partial r^2}\right]+\frac{q'''}{(\rho C_p)_f}, \tag{5}$$

$$w\frac{\partial C}{\partial z}+u\frac{\partial C}{\partial r}+\frac{\partial C}{\partial t}=D_B\left[\frac{\partial^2 C}{\partial r^2}+\frac{\partial^2 C}{\partial z^2}+\frac{1}{r}\frac{\partial C}{\partial r}\right]-k_r^2\left(\frac{T}{T_\infty}\right)^n exp\left(\frac{-E_a}{KT}\right)(C-C_\infty). \tag{6}$$

Equation (1) is the continuity equation, where u, v and w denote the velocity components, while r and z represent the coordinates. Equations (2)−(4) explain the momentum transport in the radial, tangential and axial directions. The time derivative terms refer to the presence of unsteady flow behaviour, and the convective terms are the consequences of transporting momentum because of fluid motion. Equation (2) represents the radial momentum equation. The term $\partial u/\partial t$ denotes the unsteady radial velocity, while $u\,\partial u/\partial r$ and $w\,\partial u/\partial z$ represent convective acceleration. The term $1/\rho_f\,\partial p/\partial r$ corresponds to the pressure force, and $-v^2/r$ represents the centrifugal effect due to the tangential velocity v. The terms containing ν_f describe viscous diffusion. Equation (3) is the tangential momentum equation. The term $\partial v/\partial t$ represents the unsteady tangential velocity, while $u\,\partial v/\partial r$ and $w\,\partial v/\partial z$ denote convection. The term uv/r represents the curvature effect. The viscous terms describe momentum diffusion, and the magnetic term represents resistive force. Equation (4) represents the axial momentum equation. The term $\partial w/\partial t$ denotes unsteady axial velocity, while $u\,\partial w/\partial r$ and $w\,\partial w/\partial z$ represent convection. The term $1/\rho_f\,\partial p/\partial z$ represents pressure force. The viscous terms describe momentum diffusion. Equation (5) represents the energy equation. The term $\partial T/\partial t$ denotes unsteady temperature, while $u\,\partial T/\partial r$ and $w\,\partial T/\partial z$ represent heat convection. The diffusion terms describe heat conduction, and $q'''/(\rho C_p)_f$ represents a non-uniform heat source/sink term. Equation (6) represents the concentration equation. The term $\partial C/\partial t$ denotes unsteady concentration, while $u\,\partial C/\partial r$ and $w\,\partial C/\partial z$ represent species convection. The diffusion terms describe molecular diffusion, and the last term represents the chemical reaction with activation energy.

The related boundary conditions are depicted as follows (see [42]):

- at z = 0

$$v=\frac{r\Omega_0}{(1-\alpha t)},\qquad u=\frac{rc}{(1-\alpha t)},\qquad w=w_0,$$

$$-k_f\frac{\partial T}{\partial z}=(T_w-T)h_f,\qquad C=C_w, \tag{7a}$$

- at $z\to\infty$

$$u\to 0,\qquad p\to 0,\qquad v\to 0,$$

$$T\to T_\infty,\qquad C\to C_\infty. \tag{7b}$$

Here, w_0 is the suction velocity and $r\Omega_0/(1-\alpha t)$ angular velocity with angular velocity variation α, and h_f is the HT coefficient.

The N-HSS q''' is given as follows:

$$q'''=\frac{k_f\Omega_0}{\nu_f(1-\alpha t)}[(T-T_\infty)B^*+A^*(T_w-T_\infty)F'(\eta)]. \tag{8}$$

The suitable similarity variables are introduced as follows:

$$\left.\begin{aligned} u &= F(\eta)\frac{r\Omega_0}{(1-\alpha t)}, \qquad v = G(\eta)\frac{r\Omega_0}{(1-\alpha t)},\\ w &= -2\sqrt{\frac{\nu_f\Omega_0}{(1-\alpha t)}}H(\eta), \qquad p = P(\eta)\left(\frac{-\rho_f\nu_f\Omega_0}{(1-\alpha t)}\right),\\ T &= T_\infty + (T_w - T_\infty)\theta(\eta), \qquad \eta = z\sqrt{\frac{\Omega_0}{\nu_f(1-\alpha t)}},\\ C &= C_\infty + (C_w - C_\infty)\phi(\eta). \end{aligned}\right\} \tag{9}$$

Utilising Eqs. (9), the governing Eqs. (1)–(6) are reduced and obtained as follows:

$$H' - F = 0, \tag{10}$$

$$\left(\frac{1+\beta_1}{1+\beta_2}\right)F'' + 2HF' - MF - F^2 + G^2 - \alpha^*\left[\frac{\eta}{2}F' + F\right] = 0, \tag{11}$$

$$\left(\frac{1+\beta_1}{1+\beta_2}\right)G'' - \alpha^*\left[G + \frac{\eta}{2}G'\right] + 2HG' - 2FG - MG = 0, \tag{12}$$

$$2\left(\frac{1+\beta_1}{1+\beta_2}\right)F' + 4FH - P' - \alpha^*[H + \eta H'] = 0, \tag{13}$$

$$\frac{1}{\mathrm{Pr}}\theta'' + 2H\theta' - \frac{1}{2}\alpha^*\eta\theta' + \frac{1}{\mathrm{Pr}}[\mathrm{A}^*F' + \mathrm{B}^*\theta] = 0, \tag{14}$$

$$\frac{1}{\mathrm{Sc}}\phi'' - \frac{1}{2}\alpha^*\eta\phi' + 2H\phi' - \sigma^*(1+\delta\theta)^n\, exp\left[-\frac{E}{(1+\delta\theta)}\right]\phi = 0. \tag{15}$$

The following are the modified boundary conditions:

- at $\eta = 0$

$$\begin{aligned} &F(\eta) = \gamma_1, \quad H(\eta) = \mathrm{A}, \quad G(\eta) = 1,\\ &\theta'(\eta) = -\mathrm{Bi}\big(1 - \theta(\eta)\big), \quad \phi(\eta) = 1, \end{aligned} \tag{16}$$

- as $\eta \to \infty$

$$F(\eta) = 0, \quad G(\eta) = 0, \quad P(\eta) = 0,$$
$$\theta(\eta) = 0, \quad \phi(\eta) = 0,$$

where:

$$M = \frac{\sigma_f B_0^2}{\rho_f\Omega_0}, \qquad \mathrm{Bi} = \frac{h_f}{k_f}\sqrt{\frac{\nu_f(1-\alpha t)}{\Omega_0}}, \qquad \mathrm{Pr} = \frac{(\mu C_p)_f}{k_f},$$
$$\alpha^* = \frac{\alpha}{\Omega_0}, \qquad \mathrm{Sc} = \frac{\nu_f}{D_B}, \qquad \mathrm{E} = \frac{E_a}{KT_\infty}, \qquad \gamma_1 = \frac{c}{\Omega_0},$$
$$\delta = \frac{T_w - T_\infty}{T_\infty}, \qquad \sigma^* = \frac{k_r^2(1-\alpha t)}{\Omega_0}, \qquad \mathrm{A} = \frac{-w_0}{2\sqrt{\frac{\nu_f\Omega_0}{1-\alpha t}}}.$$

where M is the magnetic parameter, Bi is the Biot number, Pr is the Prandtl number, α^* is the dimensionless quantity, Sc is the Schmidt number, E is the dimensionless activation energy, γ_1 is the stretching ratio parameter, δ is the temperature difference parameter, σ^* is the chemical reaction rate parameter, and A is a constant. Also, $F(\eta)$, $G(\eta)$, and $H(\eta)$, denote the dimensionless velocity profiles, while $\theta(\eta)$ and $\phi(\eta)$ represent the dimensionless temperature and concentration profiles, respectively.

The engineering coefficients are given as (see [43]):

$$\begin{aligned} \frac{\mathrm{Cf}}{\mathrm{Re}^{1/2}} &= \sqrt{\big(G'(0)\big)^2 + \big(F'(0)\big)^2},\\ \frac{\mathrm{Nu}}{\mathrm{Re}^{1/2}} &= -\theta'(0),\\ \frac{\mathrm{Sh}}{\mathrm{Re}^{1/2}} &= -\chi'(0). \end{aligned} \tag{17}$$

3. Methodology

FDM delineates the stability differential equations (DEs) pertinent to the discussed problem in connection with the finite element method that simulates the physical system. To accomplish this approximation, the derivatives contained in the DEs are substituted with approximations of the derivatives expressed in the DEs. The representation generated is a set of simultaneous algebraic equations. Because it directly relates to DE, FDM is a type of derivative solver. FDM can be utilised to numerically solve the system of Eqs. (10−15) and Eq. (16) for different values of the constraints. To accomplish it, consider the derivatives of ϕ, H, θ, F and G with respect to η, and imagine the solutions of ϕ, H, θ, G, P and F are χ_i, h_i, Θ_i, τ_i, p_i and ς_i, respectively, and at the points (η_i), with $i = 0, \ldots, n$

$$G' \simeq \frac{\tau_{i+1}-\tau_{i-1}}{2\Delta}, \qquad F' \simeq \frac{\varsigma_{i+1}-\varsigma_{i-1}}{2\Delta}, \qquad \theta' \simeq \frac{\Theta_{i+1}-\Theta_{i-1}}{2\Delta}$$
$$H' \simeq \frac{h_{i+1}-h_{i-1}}{2\Delta}, \qquad \phi' \simeq \frac{\chi_{i+1}-\chi_{i-1}}{2\Delta}.$$
$$G'' \simeq \frac{\tau_{i-1}-2\tau_i+\tau_{i+1}}{\Delta^2}, \qquad F'' \simeq \frac{\varsigma_{i-1}-2\varsigma_i+\varsigma_{i+1}}{\Delta^2},$$
$$\theta'' \simeq \frac{\Theta_{i-1}-2\Theta_i+\Theta_{i+1}}{\Delta^2}, \qquad H'' \simeq \frac{h_{i-1}+h_{i+1}-2h_i}{\Delta^2},$$
$$\phi'' \simeq \frac{\chi_{i-1}-2\chi_i+\chi_{i+1}}{\Delta^2}, \qquad P' \simeq \frac{p_{i+1}-p_{i-1}}{2\Delta}.$$

Using the terms mentioned here in place of the simplified equations and boundary conditions, one can obtain:

$$\frac{-h_{i-1}+h_{i+1}}{2\Delta} - \varsigma_i = 0, \tag{18}$$

$$\frac{\varsigma_{i-1}-2\varsigma_i+\varsigma_{i+1}}{\Delta^2}\left(\frac{1+\beta_1}{1+\beta_2}\right) - (\varsigma_i)^2 + (\tau_i)^2 - M\varsigma_i + 2h_i\frac{\varsigma_{i+1}-\varsigma_{i-1}}{2\Delta} - \left[\varsigma_i + \left(\frac{i\Delta}{2}\right)\frac{\varsigma_{i+1}-\varsigma_{i-1}}{2\Delta}\right]\alpha^* = 0, \tag{19}$$

$$\frac{\tau_{i+1}+\tau_{i-1}-2\tau_i}{\Delta^2}\left(\frac{1+\beta_1}{1+\beta_2}\right) + 2h_i\frac{\tau_{i+1}-\tau_{i-1}}{2\Delta} - M\tau_i - \alpha^*\left[\tau_i + \left(\frac{i\Delta}{2}\right)\frac{\tau_{i+1}-\tau_{i-1}}{2\Delta}\right] - 2\varsigma_i\tau_i = 0, \tag{20}$$

$$2\left(\frac{1+\beta_1}{1+\beta_2}\right)\frac{\varsigma_{i+1}-\varsigma_{i-1}}{2\Delta} + 4\varsigma_i h_i - \frac{p_{i+1}-p_{i-1}}{2\Delta} - \alpha^*\left[h_i + i\Delta\frac{h_{i+1}-h_{i-1}}{2\Delta}\right] = 0, \tag{21}$$

$$\left(\frac{1}{\mathrm{Pr}}\right)\frac{\Theta_{i+1}+\Theta_{i-1}-2\Theta_i}{\Delta^2} + 2h_i\left(\frac{-\Theta_{i-1}+\Theta_{i+1}}{2\Delta}\right) - \frac{1}{2}\alpha^* i\Delta\frac{\Theta_{i+1}-\Theta_{i-1}}{2\Delta} + \frac{1}{\mathrm{Pr}}\left[\mathrm{A}^*\ \frac{\varsigma_{i+1}-\varsigma_{i-1}}{2\Delta} + \mathrm{B}^*\Theta_i\right] = 0, \tag{22}$$

$$\left(\frac{1}{\mathrm{Sc}}\right)\frac{\chi_{i-1}-2\chi_i+\chi_{i+1}}{\Delta^2}+2h_i\frac{\chi_{i+1}-\chi_{i-1}}{2\Delta}-\frac{1}{2}\alpha^* i\Delta\left(\frac{-\chi_{i-1}+\chi_{i+1}}{2\Delta}\right)-\sigma^*(1+\delta\Theta_i)^n\, exp\left[-\frac{\mathrm{E}}{(1+\delta\Theta_i)}\right]\chi_i=0. \quad (23)$$

The following are the simplified boundary conditions:

$$\varsigma_0=\gamma_1,\ \ \tau_0=1,\ \ h_0=\mathrm{A},\ \ \chi_0=1,\ \ \frac{\Theta_1-\Theta_{-1}}{2\Delta}=-\mathrm{Bi}(1-\Theta_0),$$

$$\Theta_n=0,\ \ \varsigma_n=0,\ \ \tau_n=0,\ \ p_n=0,\ \ \chi_n=0. \quad (24)$$

The FDM reduces the potential energy function by simulating the solution to the controlling DEs. These equations give the requirements for carrying out the operation. To minimise the potential energy functional, the FDM gives a reasonably close answer. Table 1 presents the assessment of $-\theta'(0)$, $-G'(0)$ and $F'(0)$ results with an established study for a reduced case. Figure 2 depicts the flow chart of the numerical procedure.

Table 1. The assessment of $-\theta'(0)$, $-G'(0)$ and $F'(0)$ results with an established study, for some reduced cases.

	Turkyilmazoglu [44]	Present results
$-\theta'(0)$	0.93387794	0.93388563
$-G'(0)$	0.61592201	0.61591889
$F'(0)$	0.51023262	0.51024235

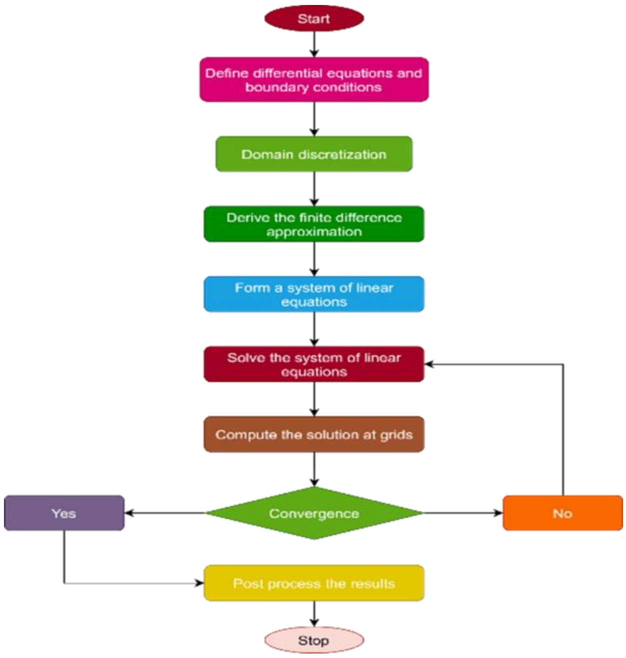

Fig. 2. Flowchart of the numerical procedure.

4. Artificial neural networks

ANNs are an essential instrument for modelling and predicting complex systems. ANNs are particularly beneficial in this scenario since they can identify the essential patterns and relationships within the data, allowing more precise predictions of fluid dynamics and thermal behaviour. By being trained on a set of data, the network could uncover the complex connections between the output variables and the input parameters. ANNs are capable of handling large datasets and identifying complex patterns that traditional mathematical modelling approaches would overlook. ANNs are also proficient in processing massive amounts of data. The ANN structure for the profiles $-\theta'(0)$, $-G'(0)$ and $F'(0)$ are seen in the figures. The correctness of the supplied data is ensured through comparison analysis.

ANNs can be expressed mathematically as:

$$A=\sum_{j=0}^{N}Q_i\xi_i+C_0. \quad (25)$$

Here, N is the number of inputs, ξ_i is the input value, and C_0 and Q_i represent the bias and weight.

The regression (R^2) and mean square error (MSE) equations are quantified as follows:

$$R^2=1-\left(\frac{\sum_{i=1}^{j}\left(-\delta_{ANN(i)}+\delta_{NUM(i)}\right)^2}{\sum_{i=1}^{j}\left(\delta_{NUM(i)}\right)^2}\right), \quad (26)$$

$$MSE=\frac{1}{j}\sum_{i=1}^{j}\left(-\delta_{ANN(i)}+\delta_{NUM(i)}\right). \quad (27)$$

5. Response surface methodology

RSM is a statistical method that predicts and maximises the connections between different input components and outcome features. The effect of the Biot number, A^* and B^* on the Nusselt number is examined using RSM for thermal transfer analysis. To evaluate the correctness of the research, analysis of variance (ANOVA) employs statistical measures, including p-values, F-values, error rates and lack-of-fit tests. If the F-value is greater than 1 and the p-value is less than 0.05, the accuracy is confirmed at the 95% confidence level. This study confirms that the regression model accurately predicts the Nusselt number by accounting for all relevant inputs. The model's correctness is confirmed by residual and distribution analyses, as well as the correlation between adjusted and predicted values. This method is effective at evaluating massive non-linear interactions, and offers significant techniques for maximising or limiting responses. The response is modelled using the necessary parameters using the traditional multivariate design, which is explained below:

$$\mathrm{Nu}\ =\ \Upsilon_1+\Upsilon_2A+\Upsilon_3B+\Upsilon_4C+\Upsilon_5A\cdot A+\Upsilon_6B\cdot B+$$
$$+\Upsilon_7C\cdot C+\Upsilon_8A\cdot B+\Upsilon_9A\cdot C+\Upsilon_{10}\,B\cdot C \quad (28)$$

Here, Υ_i $(i=1, 2, \ldots, 10)$ signifies the factors of the quadratic model resulting from RSM, which is used to assess the parameters and their interactive effects on HT.

The provided regression model contains interaction, linear and quadratic effects. The central composite design experimental framework includes centralised runs as well as axial and factorial runs. To match the square-shaped region of interest, the axis extends about one unit from the centre. Table 2 provides specifics about the effective factor range for imitating Nu. Furthermore, the regression model that corresponds to the important factorial parameters is expressed in actual units as:

Table 2. Factors coded values and their range.

Parameter	Range	Level		
		-1	0	1
A^*	-0.1 to 0.2	-0.1	0.05	0.2
B^*	-0.1 to 0.2	-0.1	0.05	0.2
Bi	0.35 to 10	0.35	5.175	10

$$\mathrm{Nu} = 0.1527 - 0.117{\cdot}\mathrm{B}^* + 0.352{\cdot}\mathrm{A}^* + 0.82{\cdot}\mathrm{A}^*{\cdot}\mathrm{A}^* + \\ + 0.1478{\cdot}\mathrm{Bi} - 0.26{\cdot}\mathrm{B}^*{\cdot}\mathrm{B}^* - 0.00955{\cdot}\mathrm{Bi}{\cdot}\mathrm{Bi} + \\ + 0.3030{\cdot}\mathrm{A}^*{\cdot}\mathrm{Bi} + 0.768{\cdot}\mathrm{A}^*{\cdot}\mathrm{B}^* - 0.0430{\cdot}\mathrm{B}^*{\cdot}\mathrm{Bi}. \quad (29)$$

5.1. Model validation

The reliability and robustness of the model are evaluated using statistical techniques such as lack-of-fit tests and ANOVA. To assess the model's ability to capture changes in the response variable, specific indicators are needed. To guarantee exceptional precision in the results, a 5% significance level or 95% confidence level is frequently utilised. Together with a model that links the response to the factors and the Nusselt number, the ANOVA results display the p-values for each of the three components. At the 95% level of significance, a parameter is considered statistically significant if its p-value is less than 0.05. Except for $A^*{\cdot}A^*$, $B^*{\cdot}B^*$, $A^*{\cdot}B^*$ and $A^*{\cdot}\mathrm{Bi}$, all terms have p-values below 0.05, so the insignificant term has been eliminated. As a result, the updated model is shown as follows:

$$\mathrm{Nu} = 0.1527 + 0.352{\cdot}\mathrm{A}^* + 0.1478{\cdot}\mathrm{Bi} + \\ - 0.00955{\cdot}\mathrm{Bi}{\cdot}\mathrm{Bi} + 0.3030{\cdot}\mathrm{A}^*{\cdot}\mathrm{Bi}. \quad (30)$$

The modified values of R^2 (97.17%) and estimated values of R^2 (98.51%) were found, along with a synopsis of the scrutiny. ANOVA was used to assess the model's dependability, and Table 3 provides specifics of the findings.

Table 3. Factor-coded values and their range.

Source	DF	Adj SS	Adj MS	F-value	P-value
B^*	1	0.02406	0.024058	6.41	0.030
Square	3	0.23158	0.077194	20.57	0.000
A^*	1	0.93709	0.937089	249.71	0.000
Model	9	2.48152	0.275724	73.47	0.000
Bi	1	0.89384	0.893843	238.19	0.000
Linear	3	1.85499	0.618330	164.77	0.000
$B^*{\cdot}B^*$	1	0.00009	0.000091	0.02	0.879
Bi·Bi	1	0.13601	0.136006	36.24	0.000
$A^*{\cdot}A^*$	1	0.00094	0.000936	0.25	0.628
2-way interaction	3	0.39495	0.131649	35.08	0.000
$A^*{\cdot}B^*$	1	0.00239	0.002391	0.64	0.443
$B^*{\cdot}$Bi	1	0.00775	0.007754	2.07	0.181
$A^*{\cdot}$Bi	1	0.38480	0.384800	102.54	0.000
Error	10	0.03753	0.003753	-	-
Pure error	5	0.00000	0.000000	-	-
Lack-of-fit	5	0.03753	0.007505	-	-
Total	19	2.51904	-	-	-

6. Results and discussion

This research analyses the motion of Boger liquid around a slowly revolving stretching disk with the effect of an MF. The consequence of N-HSS, C-BCs and AE on the motion of the liquid is also considered. The governing PDEs are converted to ODEs with the aid of similarity variables. The resulting ODEs are solved by using the FDM scheme. Additionally, ANN is used to examine the mass, heat and liquid flow transport properties, and the obtained ANN graphs for $F(\eta)$, $\theta(\eta)$ and $\phi(\eta)$ are depicted with the appropriate results. Additionally, the Nusselt number was evaluated for different parameters using RSM. The graphical representation reveals many dimensionless factors influencing the different profiles.

The consequences of β_1 on $F(\eta)$ and $G(\eta)$ are exposed in Fig. 3 and Fig. 4. An increased solvent fraction signifies an improvement in $G(\eta)$ and $F(\eta)$ for growing values corresponding to a greater solvent ratio relative to the fluid particles. The augmented solvent volume leads to a drop in the liquid's flow resistance and viscosity. Reduced fluid flow friction within the system results in lower viscosity and higher velocities. The reduced viscosity enhances the liquid's response to flow-driving forces, facilitating the deformation and movement of fluid layers with greater ease. Consequently, as the fluid undergoes a reduction in resistance and internal friction, both velocity components augment, which is due to the reduction in friction and resistance. The effect is most evident in Boger fluids, which exhibit a constant viscosity irrespective of the shear rate.

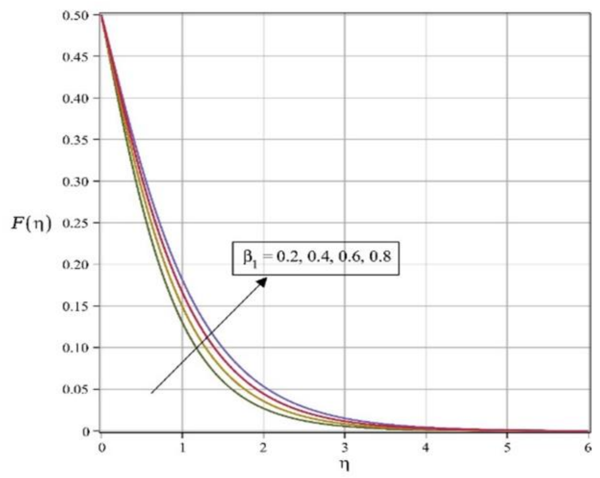

Fig. 3. The effect of β_1 on $F(\eta)$.

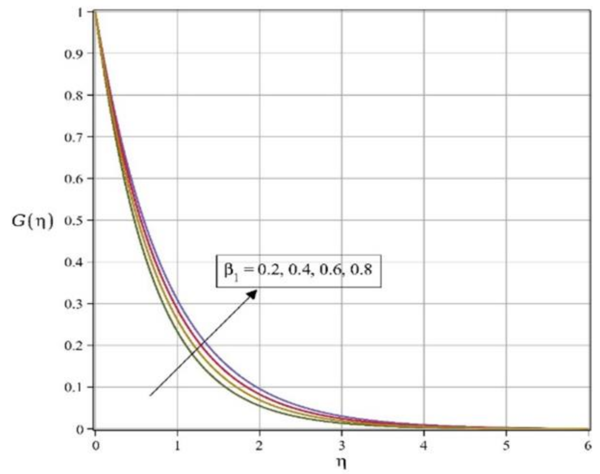

Fig. 4. The effect of β_1 on $G(\eta)$.

Figures 5 and 6 illustrate the outcome of M on $F(\eta)$ and $G(\eta)$. It is observed that both velocity profiles drop significantly as the MF strength increases. The M is related to the Lorentz force.

Physically, increasing the M value lowers the velocity by increasing the Lorentz force, causing the liquid's motion to slow. The resistive force in speed and amplitude causes the fluid's velocity to decrease. MF effectively limits the flow because it opposes the flow's driving forces, which lowers $F(\eta)$ and $G(\eta)$.

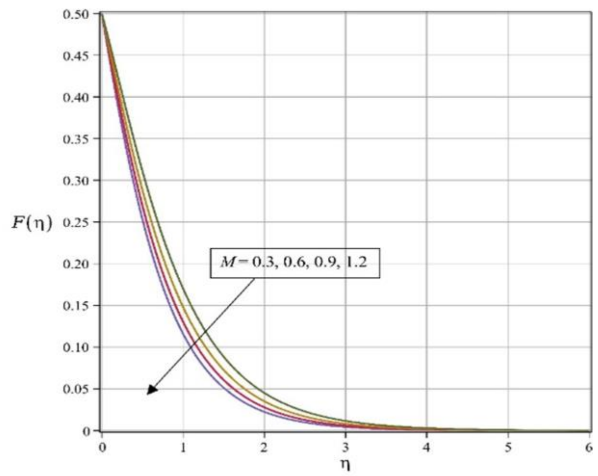

Fig. 5. The effect of M on $F(\eta)$.

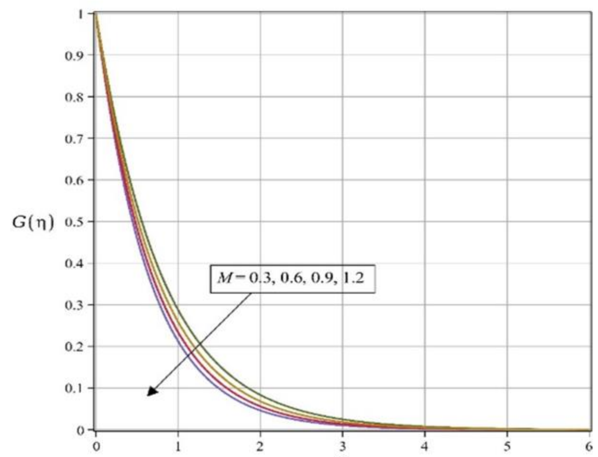

Fig. 6. The effect of M on $G(\eta)$.

The impact of β_2 on $F(\eta)$ and $G(\eta)$ is revealed in Fig. 7 and Fig. 8, respectively. $G(\eta)$ and $F(\eta)$ drop for increased values of β_2. An increase in β_2 indicates an extended liquid relaxation duration compared to the flow's time scale. The liquid's slow reaction to distortion, attributable to its extended relaxation period, clearly demonstrates its viscoelastic characteristics. Consequently, the fluid exhibits greater resistance to distortion and motion. However, its ability to adapt to variations in dynamic flow is limited. In both velocity profiles, the liquid is less susceptible to shear forces due to the resistance. By prolonging the relaxation time, the fluid's velocity components are effectively reduced, leading to decreased flow rates. As the liquid's viscoelastic resistance rises, both velocity profiles decrease.

Figures 9 and 10 demonstrate the impact of A on $F(\eta)$ and $G(\eta)$. The intensification in the values of A causes reductions of both $G(\eta)$ and $F(\eta)$. When they get close to the surface, the velocities drastically decrease. An increase in A implies stronger fluid withdrawal from the flow region. This retards the momentum of the fluid and makes the velocity boundary layer thinner, which results in a decreased value of $F(\eta)$ and $G(\eta)$.

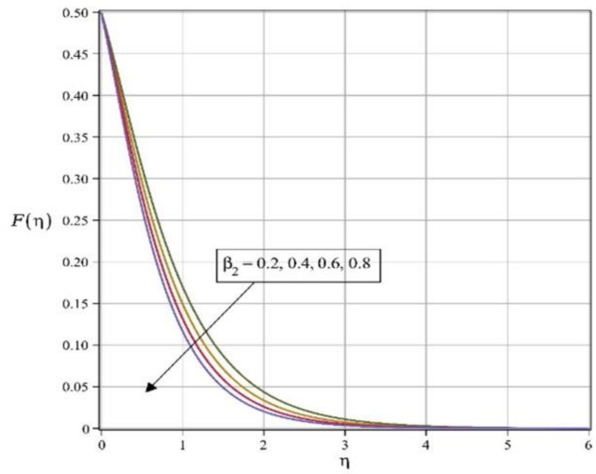

Fig. 7. The effect of β_2 on $F(\eta)$.

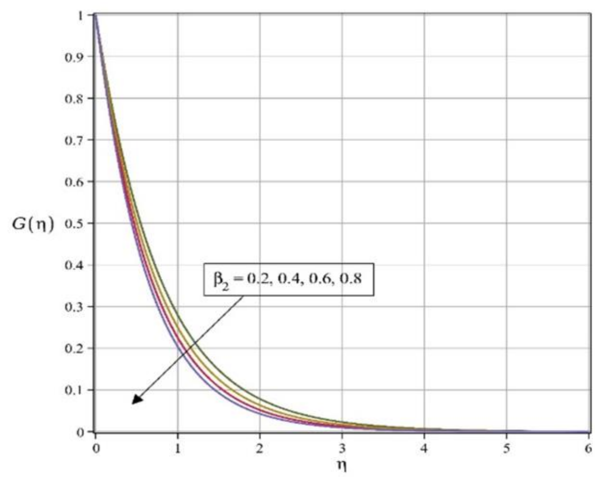

Fig. 8. The effect of β_2 on $G(\eta)$.

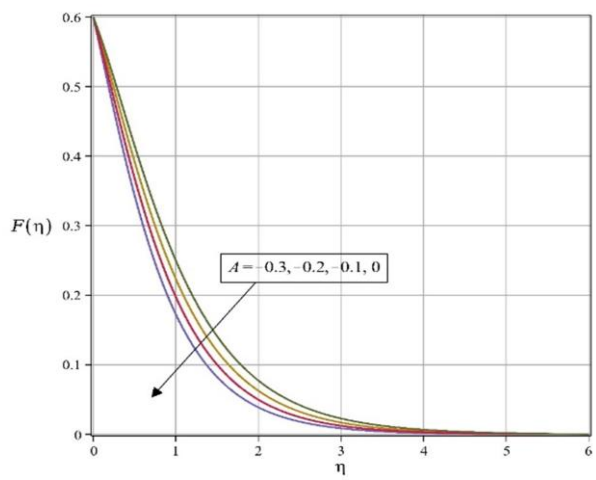

Fig. 9. The effect of A on $F(\eta)$.

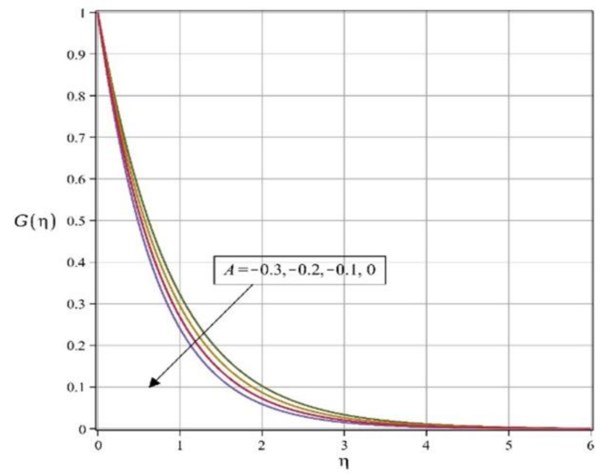

Fig. 10. The effect of A on $G(\eta)$.

Figures 11 and 12 demonstrate the significance of A^* and B^* for $\theta(\eta)$, respectively. $\theta(\eta)$ is growing due to the elevated values of N-HSS parameters (A^*, B^*).

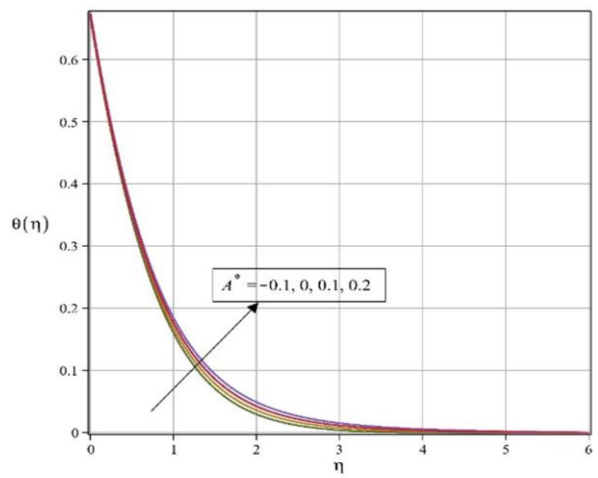

Fig. 11 The effect of A^* on $\theta(\eta)$.

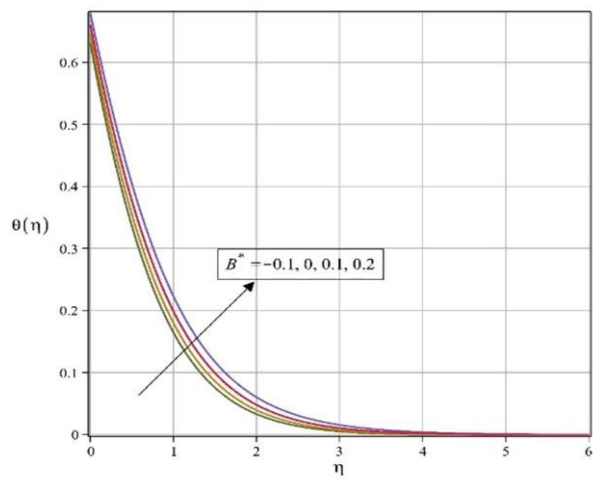

Fig. 12. The effect of B^* on $\theta(\eta)$.

The positive values of A^* and B^* can be read physically as heat sources that function as heat producers, resulting in the release of heat energy into the stream and an increase in $\theta(\eta)$. The negative values of B^* and A^* indicate the heat sink, which functions as a heat absorber, with energy being absorbed for these negative values. Figure 13 demonstrates the effect of Bi on $\theta(\eta)$. The thermal profile advances with the increase in Bi values. The relationship between temperature and temperature boundary layer thickness correlates strongly with Bi. The heat transport coefficient is crucial for Bi, its value escalates with a rise in the heat transmission coefficient. Consequently, elevated heat transport coefficient values lead to the enhanced temperature and boundary layer thickness.

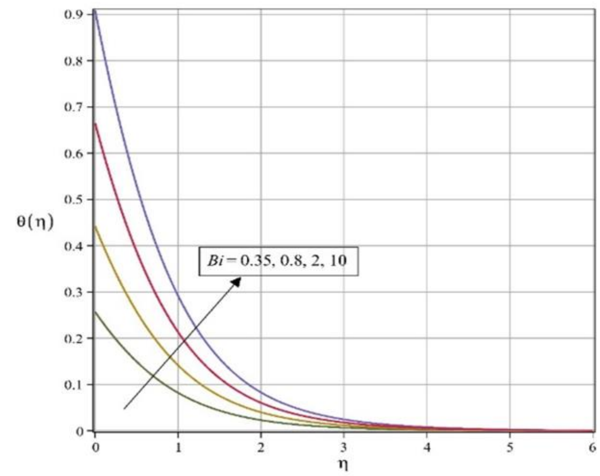

Fig. 13. The effect of Bi on $\theta(\eta)$.

Figure 14 demonstrates the significance of σ^* for $\phi(\eta)$. The increasing σ^* values decrease the concentration profile. As the chemical reaction rises, it quickly increases the concentration of reactants near the reacting surface. As those reactant particles get depleted, the difference in concentration that pushes them to move from one place to another becomes smaller. Since this concentration difference drives mass transfer, its reduction slows down the overall transport of material. Overall, stronger reactions exhaust the reactants too fast, leaving less to be carried forward, which ultimately weakens mass transfer. The effect of E on the $\phi(\eta)$ is exhibited in Fig. 15.

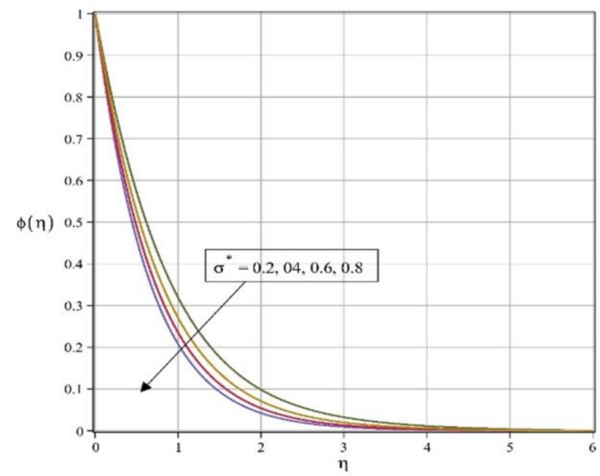

Fig. 14. The effect of σ^* on $\phi(\eta)$.

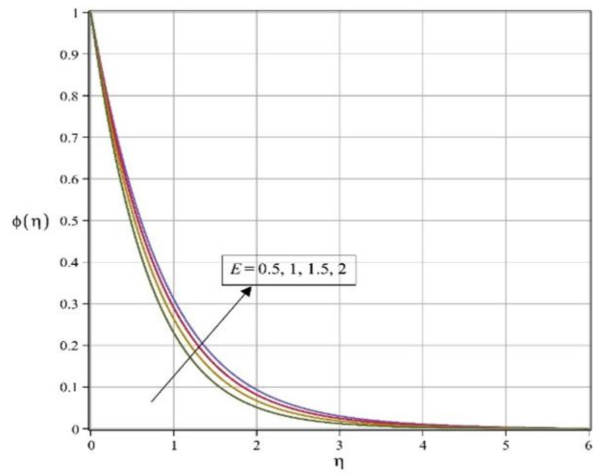

Fig. 15. The effect of E on $\phi(\eta)$.

The mass transfer is advanced by the increase in E. A low AE has been shown to decrease the reaction rate, which in turn causes chemical reaction mechanisms to decay. The improved Arrhenius process declines with increasing E. Thus, this accelerates the generative chemical process, raising the nanoparticle concentration. Figure 16 represents the effect of Sc on $\phi(\eta)$. The increased value of Sc declines the $\phi(\eta)$ profile. A higher Sc means that the fluid's momentum spreads much faster than its mass does. When the mass diffusivity becomes low, the species cannot disperse easily through the liquid. As a result, the concentration gradient remains steep near the surface, and the overall concentration level decreases throughout the boundary layer. Therefore, an increase in Sc causes a noticeable drop in $\phi(\eta)$.

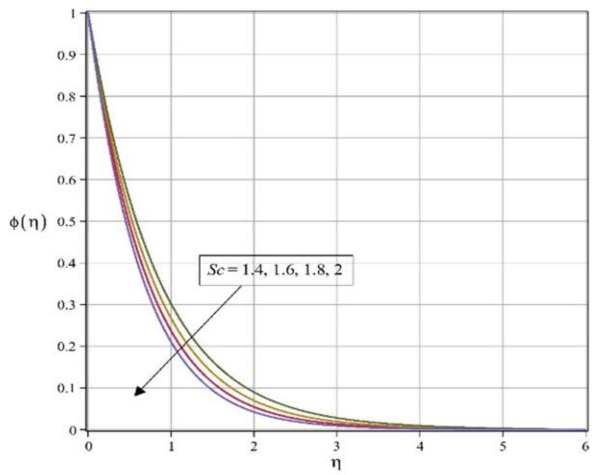

Fig. 16. The effect of Sc on $\phi(\eta)$.

Figures 17, 18, and 19 show the impact of β_2, γ_1 and M on the isotherms. A larger β_2 and γ_1 value often causes more affected bending of the isotherms, which modifies the stream pattern of the disk. This effect may enhance or impair the liquid's mixing and transport properties, depending on the application. Additionally, complex flow behaviours that are essential for optimising processes like magnetic resonance imaging and magnetic drug targeting may arise from the interaction of the MF parameter. The increased effective diffusivity lessens changes in the concentration gradient. The increased depletion of reactants as Sc increases, owing to reduced mass diffusivity, results in a fall in $\phi(\eta)$. Tables 4 and 5 depict values of C_f and Nu for various values of different parameters.

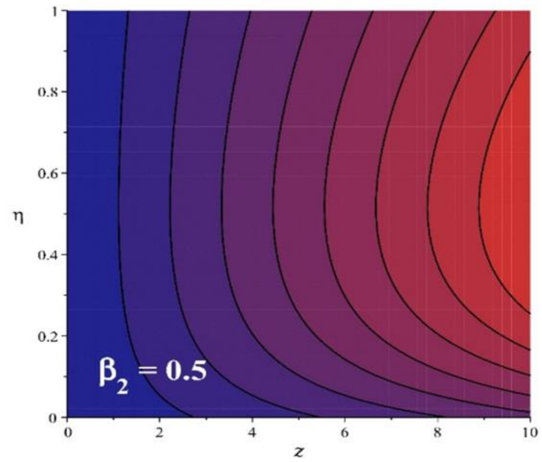

Fig. 17. The effect of β_2 on isotherms.

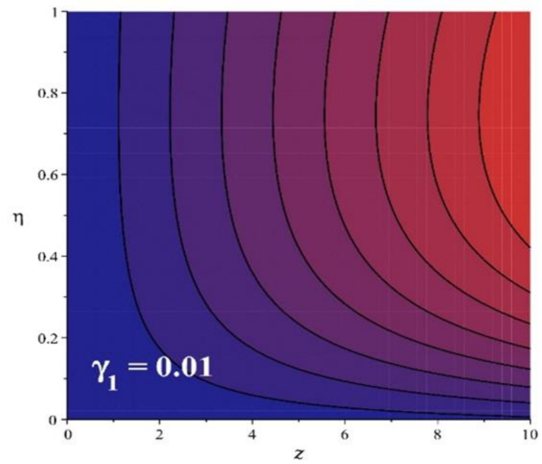

Fig. 18. The effect of γ_1 on isotherms.

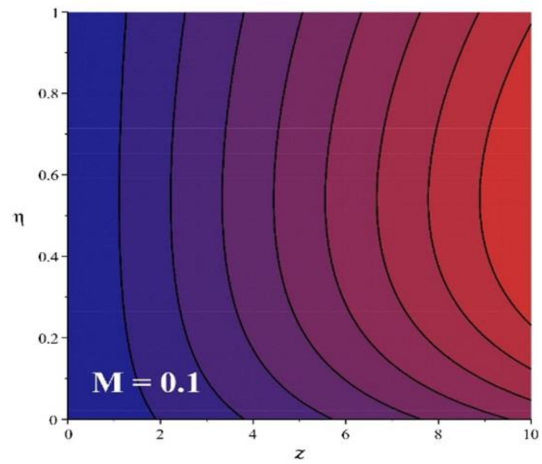

Fig. 19. The effect of M on isotherms.

Table 4. Values of C_f for several values of different parameters.

β_1	β_2	M	α^*	A	γ_1	C_f
0.1						1.042287
0.2	0.1	0.1	0.1	0.2	0.1	0.990247
0.3						0.944963
	0.2					1.097463
0.1	0.4	0.1	0.1	0.2	0.1	1.20364
	0.6					1.305283
		0.1				1.092923
0.2	0.3	0.2	0.1	0.2	0.1	1.133078
		0.3				1.17445
			0.1			1.184868
0.2	0.2	0.2	0.2	0.3	0.1	1.214202
			0.3			1.243693
				0.1		1.053558
0.1	0.1	0.1	0.1	0.2	0.2	1.151923
				0.3		1.262031
					0.1	1.331356
0.1	0.1	0.1	0.2	0.4	0.2	1.412899
					0.3	1.508619

Table 5. Values of Nu for several values of different parameters.

M	α^*	A*	B*	Bi	Nu
0.1					0.744257
0.2	0.1	0.1	0.1	1	0.743091
0.3					0.742016
	0.1				0.745093
0.1	0.2	0.2	0.2	1	0.738799
	0.3				0.731253
		0.1			0.740948
0.1	0.2	0.2	0.3	1	0.739542
		0.3			0.738136
			0.1		0.739161
0.3	0.1	0.3	0.2	1	0.741271
			0.3		0.743311
					0.096555
0.1	0.1	0.1	0.1	0.1	0.186934
					0.271711

ANNs are an extremely flexible modelling tool that can be used to solve a wide range of classification or prediction issues. They can comprehend the accurate relationship between output and data. Within an ANN architecture, output and input neurons are connected by various layers of neurons, including hidden layers. Initial training and evaluation of ANNs are based on empirical data to control the optimal topology and weights. ANNs use the back-propagation approach to adjust their weights during training to decrease the differences between predicted and actual outcomes. The input, output and hidden layers of neurons comprise ANNs. The data is divided as 80% goes into the training database, 10% into the validation database, and 10% into the testing database.

Figure 20 depicts the ANN design, consisting of an input, hidden, and output layer.

Figures 21(a), 22(a) and 23(a) show MSE for $F(\eta)$, $\theta(\eta)$ and $\phi(\eta)$ profiles in the rotating disk configuration, accounting for the testing, validation and training phases. The best efficiency is obtained with MSE values of 1.0118E-14, 1.4356E-10 and 3.0595E-11 for 133, 833 and 908 epochs, respectively. Since MSE calculates the difference between the ideal outcomes and the intended solutions, the lowest MSE values indicate precise and effective outcomes.

Figures 21(b), 22(b) and 23(b) show the training state for $F(\eta)$, $\theta(\eta)$ and $\phi(\eta)$. As seen in Figs. 21(b), 22(b) and 23(b), the gradient parameter is 9.8743E-08 for 133 epochs, 9.9822E-08 for 833 epochs and 9.9726E-08 for 908 epochs of $F(\eta)$, $\theta(\eta)$ and $\phi(\eta)$ profiles, correspondingly. The Mu parameter of ANN is 1E-14 for 133 epochs, 1E-08 for 833 epochs and 1E-09 for 908 epochs of $F(\eta)$, $\theta(\eta)$ and $\phi(\eta)$ profiles. The validation checks are zero for all profiles. The results of the procedure demonstrated that the built ANN actively converged and was accurate.

The histograms of error for the $F(\eta)$, $\theta(\eta)$ and $\phi(\eta)$ profiles are shown in Figs. 21(c), 22(c), and 23(c). The zero error line for $F(\eta)$, $\theta(\eta)$ and $\phi(\eta)$ is indicated by a coloured line. It is seen that the zero-error line is approximately at −5.3E-09 for $F(\eta)$, 3.52E-07 for $\theta(\eta)$ and −4.8E-07 for $\phi(\eta)$.

Figures 21(d), 22(d) and 23(d) present extensive information on regression cases for all three of the suggested model's situations. By demonstrating the linearity between the intended and actual outputs, the graphs reveal the relationship between all datasets, including training, validation and testing data. A regression value of $R = 1$ signifies an optimal fit, and the regression diagrams illustrate the degree of correspondence between the data and the curve or line for the $F(\eta)$, $\theta(\eta)$ and $\phi(\eta)$ profiles, as represented in the related figures.

The fit curve for $F(\eta)$, $\theta(\eta)$ and $\phi(\eta)$ is illustrated in Figs. 21(e), 22(e) and 23(e). Errors identified by analysing the difference between the ANN's predicted and actual outcomes are shown in Figs. 21(f), 22(f) and 23(f). The accuracy of the ANN model's implementation is reflected in the absolute error.

Figs. 24(a), 24(b) and 24(c) illustrate the comparison between ANN values and FDM results for $F(\eta)$, $\theta(\eta)$, and $\phi(\eta)$. The comparison shows a strong correlation between the values derived from the ANN method and those from the FDM results.

The regression plots for Nu are detailed in Fig. 25. The detailed analysis of the surface plots and contours is visualised in Fig. 26.

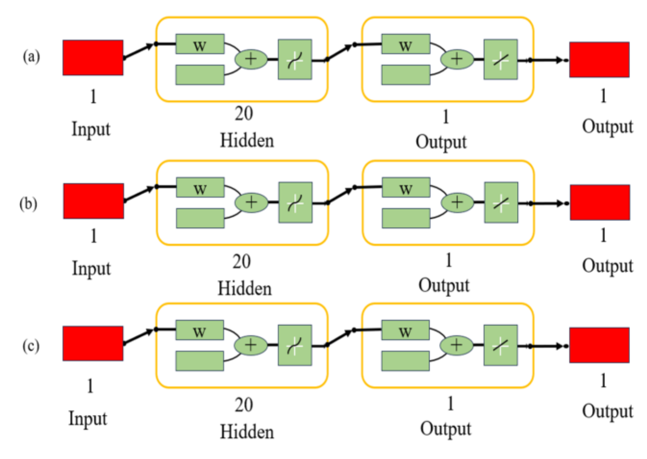

Fig. 20. ANN design.

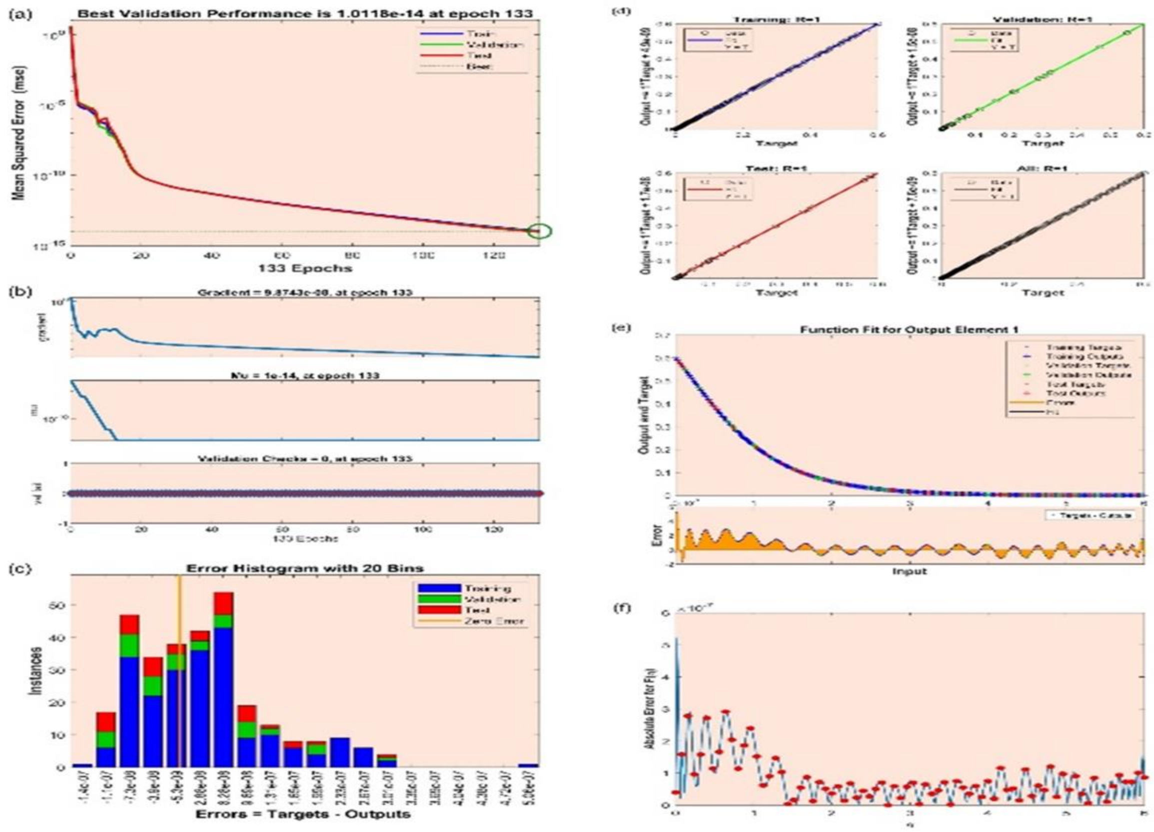

Fig. 21. Visual representation of ANN outcome of (a) performance, (b) training, (c) histogram of error, (d) regression analysis, (e) fit curve and (f) absolute error for $F(\eta)$.

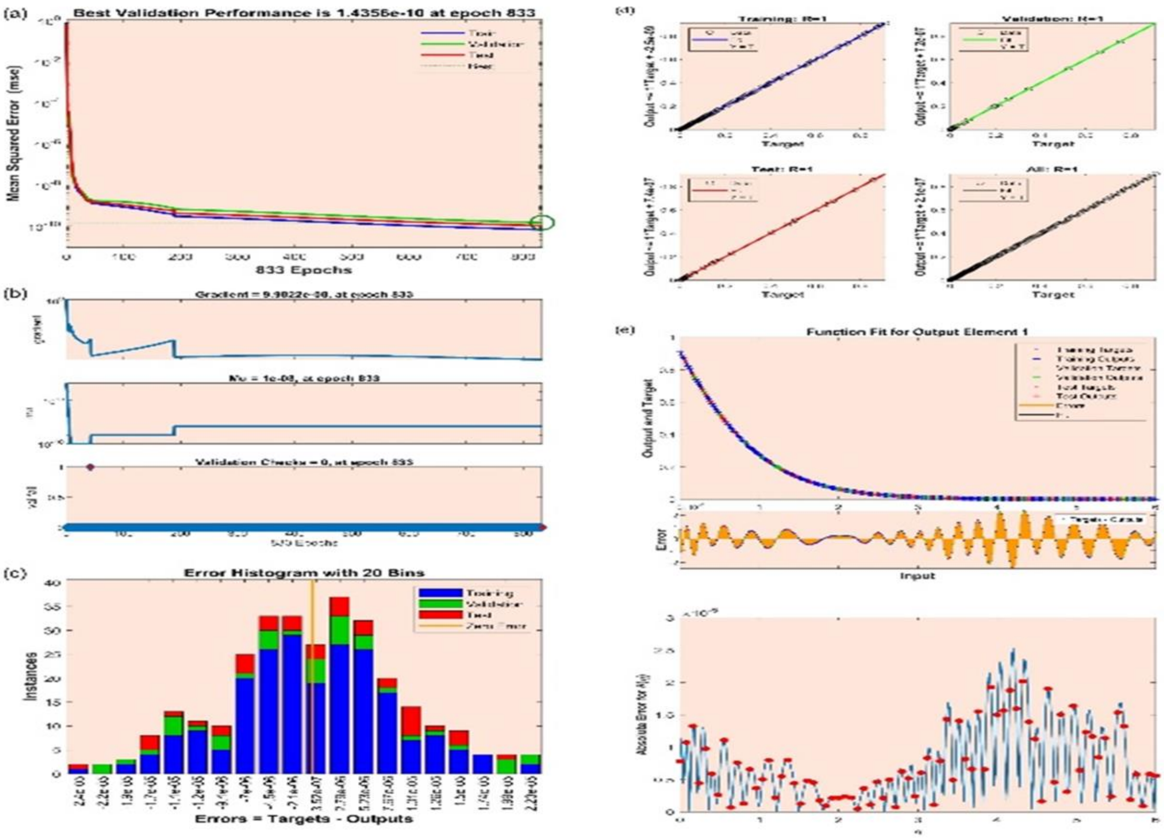

Fig. 22. Visual representation of ANN outcome of (a) performance, (b) training, (c) histogram of error, (d) regression analysis, (e) fit curve and (f) absolute error for $\theta(\eta)$.

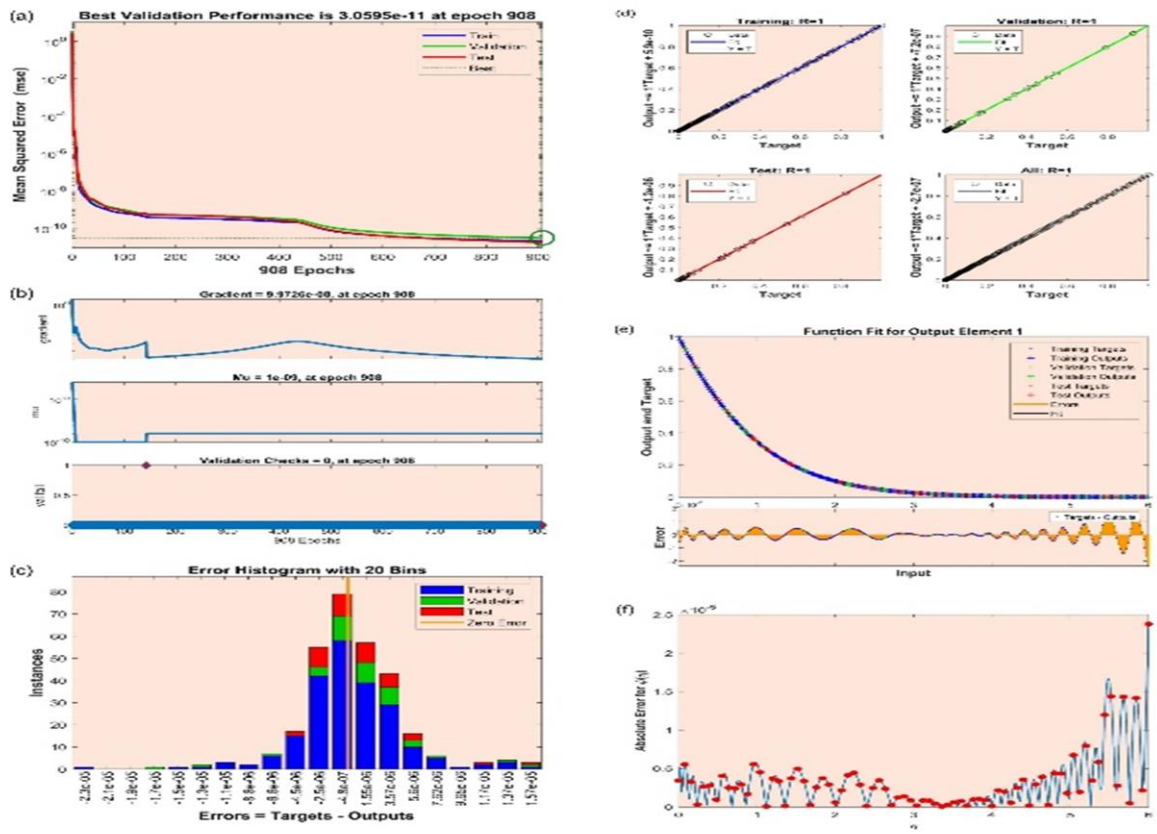

Fig. 23. Visual representation of ANN outcome of (a) performance, (b) training, (c) histogram of error, (d) regression analysis, (e) fit curve and (f) absolute error for $\phi(\eta)$.

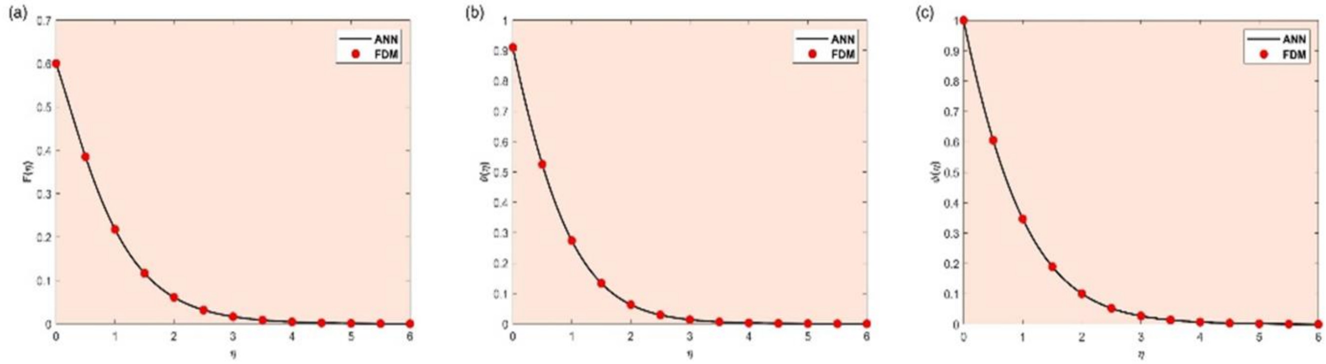

Fig. 24. Comparison of ANN results and FDM outcomes for (a) $F(\eta)$, (b) $\theta(\eta)$ and (c) $\phi(\eta)$.

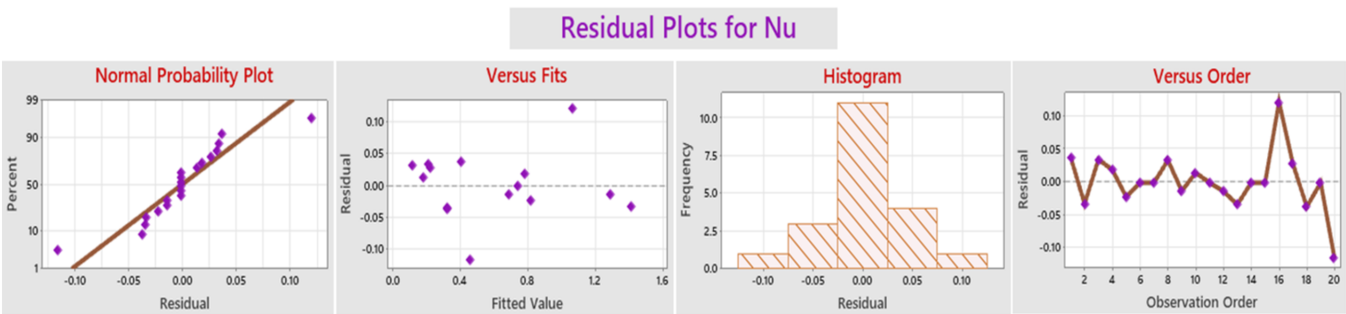

Fig. 25. Regression plots for Nu.

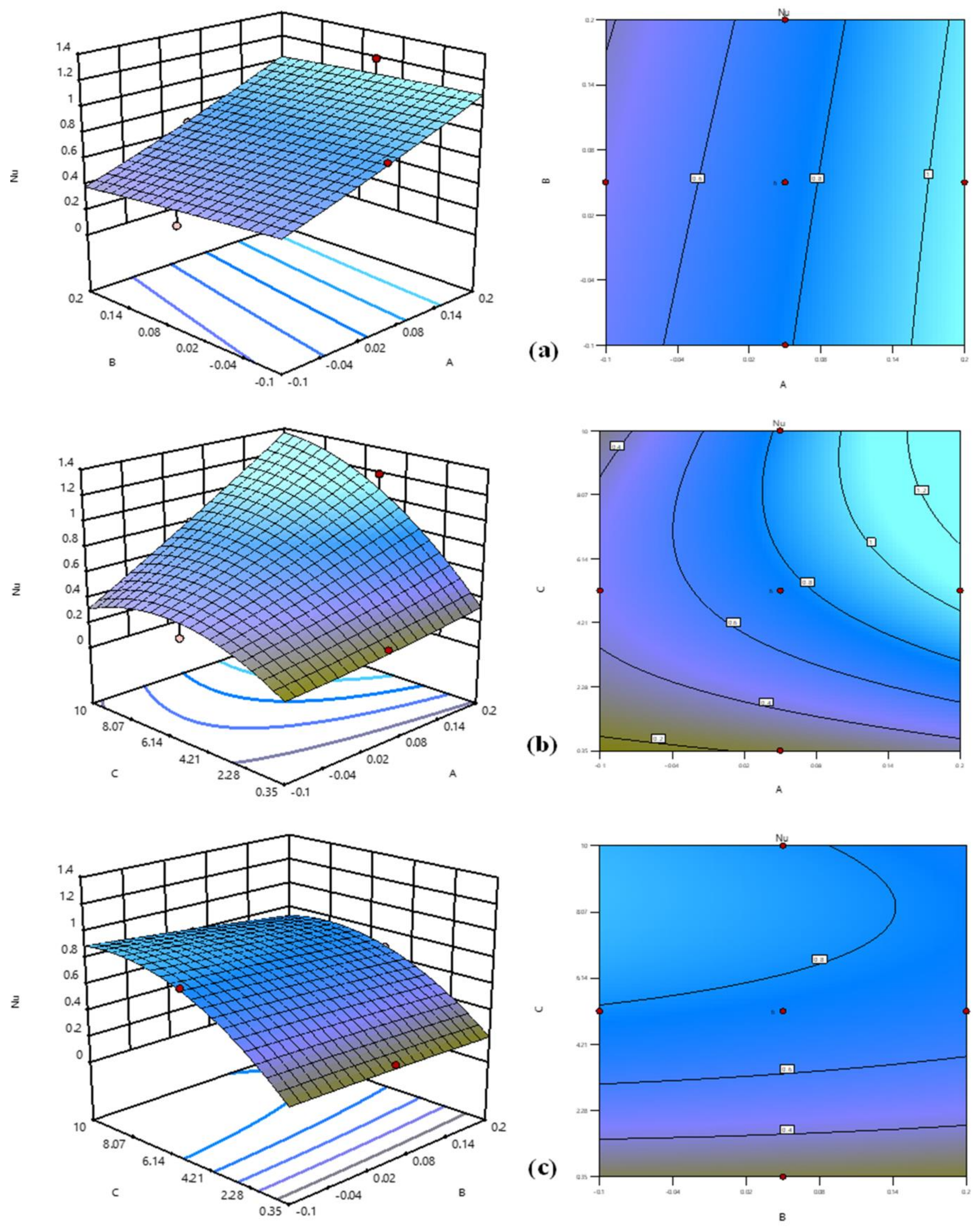

Fig. 26. Contour and surface plots for Nu

7. Conclusions

The current analysis examines the effects of AE, chemical reactions and MF on the time-dependent flow of a Boger liquid over a slowly rotating stretching disk. The analysis also accounts for the impact of suction, C-BCs and N-HSS on the liquid stream to assess the thermal behaviour. It is anticipated that the primary source of the flow's instability would be the disk's angular velocity. The decreased speed of a disk is explained by the fact that its angular velocity is inversely proportional to time. The governing PDEs are transformed into dimensionless ODEs by using similarity variables. The reduced ODEs are solved using the FDM technique. ANN is used in the study to assess the mass transport, heat transport and fluid flow characteristics. Additionally, RSM is employed to evaluate the HT rate of the fluid flow. Graphical representations show how diverse variables affect the velocity, concentration, and temperature profiles. The following are the main findings of the investigation:

- $F(\eta)$ and $G(\eta)$ decline as the β_2 rises. Reduced flow rates are the outcome of increasing the relaxation time, excellently reducing the velocity components of the fluid.
- As the magnetic parameter values increase, $F(\eta)$ and $G(\eta)$ decline. The resistive force causes the liquid velocity components to decrease in magnitude.
- An increase in β_1 enhances $F(\eta)$ and $G(\eta)$. The fluid's increased reactivity to the flow's driving forces makes the lower viscosity easier for fluid layers to move and deform.
- $\theta(\eta)$ intensifies as the A^* and B^* rise. The positive values of A^* and B^* could be interpreted physically as heat sources that generate heat, leading to the emission of thermal energy into the flow and an elevation in $\theta(\eta)$.
- As the values of Bi increase, $\theta(\eta)$ rises. The heat transport coefficient is essential to Bi, since its value increases with an elevation in the heat transportation efficiency.
- The increase in values of σ^* reduces the concentration profile. Intense chemical reactions have detrimental physical effects that diminish the reactant species, resulting in a mass transfer drop.
- The $\phi(\eta)$ upsurges as the values of E increase. Reduced AE has been shown to diminish the reaction rate, leading to chemical reaction degradation.
- The graphical representation illustrates the comparison between ANN values and FDM outputs. The comparison reveals that the results derived from the FDM and ANN approaches are in close agreement, with no significant difference between them.
- The optimisation of heat transmission is significantly influenced by factors such as the Biot number, space and temperature-dependent heat source/sink parameters.
- The current analysis with a confidence level of 95% identifies important influential components, revealing an enhanced technique for improving heat transmission.

References

[1] Chamkha, A.J., & Pop, I. (2004). Effect of thermophoresis particle deposition in free convection boundary layer from a vertical flat plate embedded in a porous medium. *International Communications in Heat and Mass Transfer*, 31(3), 421–430. doi: 10.1016/j.icheatmasstransfer.2004.02.012

[2] Kattimani, P., Prasad, K.V., Anwar, T., Jena, S.P., Shankhyan, A., & Naveen Kumar, R. (2025). Application of Levenberg-Marquardt artificial neural network to study nanoparticle aggregation phenomena in stagnation point flow towards an off-centered rotating disk. *International Journal of Thermofluids*, 27, 101276. doi: 10.1016/j.ijft.2025.101276

[3] Varun Kumar, R.S., Chandan, K., Venkadeshwaran, K., Muhammad, T., Punith Gowda, R.J., & Prasannakumara, B.C. (2025). Influence of magnetic dipole on the hybrid nanofluid flow with chemical reactions due to the generated and absorbed heat. *Pramana*, 99(2), 65. doi: 10.1007/s12043-025-02917-4

[4] Hussain, S.M., Arshad, M., Qureshi, M.A., Guedri, K., Prasad, K.V., Karthik, K., Varun Kumar, R., & Bayram, M. (2025). Entropy analysis of Casson ternary hybrid nanofluid using convective cross diffusion model via spinning sphere based artificial neural network. *Proceedings of the Institution of Mechanical Engineers, Part N: Journal of Nanomaterials, Nanoengineering and Nanosystems*, 23977914251345873. doi: 10.1177/23977914251345873

[5] Eegunjobi, A.S., Makinde, O.D., & Jangili, S. (2017). Unsteady MHD Chemically Reacting and Radiating Mixed Convection Slip Flow Past a Stretching Surface in a Porous Medium. *Defect and Diffusion Forum*, 377, 200–210. doi: 10.4028/www.scientific.net/DDF.377.200

[6] Norouzi, M., Emamian, A., & Davoodi, M. (2019). An analytical and experimental study on dynamics of a circulating Boger drop translating through Newtonian fluids at inertia regime. *Journal of Non-Newtonian Fluid Mechanics*, 267, 1–13. doi: 10.1016/j.jnnfm.2019.03.005

[7] Banakar, V.R., Patil, N., Kalia, R., Shankar, B., & Karthik, K. (2025). The role of nanoparticle diameter and solid-fluid interfacial layer behavior under low oscillating magnetic fields: A response surface methodology and ANOVA approach. *Proceedings of the Institution of Mechanical Engineers, Part N: Journal of Nanomaterials, Nanoengineering and Nanosystems*, 23977914251341443. doi: 10.1177/23977914251341443

[8] Veeranna, Y., Kattimani, P., Kulshreshta, A., Punith Gowda, R.J., & Sarris, I.E. (2025). Significance of solvent percentage and external pollutant source concentration in Boger-micropolar fluid flow across a semi-circular body. *International Journal of Thermofluids*, 29, 101399. doi: 10.1016/j.ijft.2025.101399

[9] Hue, S.H., Chagot, L., & Angeli, P. (2024). Studies of interfacial wave properties during displacement with pure viscoelastic fluids in microchannels. *Physics of Fluids*, 36(1), 013109. doi: 10.1063/5.0186036

[10] Sreehari, P., Gopal, D., Kishan, N., Venkadeshwaran, K., Singh, S., & Karthik, K. (2025). A numerical study on the radiative flow of magneto-Casson fluid via a vertical microchannel with entropy generation. *Journal of the Korean Physical Society*, 86(5), 372−382. doi: 10.1007/s40042-025-01289-7

[11] Veera Krishna, M., Ameer Ahamad, N., & Chamkha, A.J. (2021). Hall and ion slip impacts on unsteady MHD convective rotating flow of heat generating/absorbing second grade fluid. *Alexandria Engineering Journal*, 60(1), 845–858. doi: 10.1016/j.aej.2020.10.013

[12] Preethi, K., Hanumagowda, B.N., Pavithra, K.M., Varma, S.V.K., Mann, V.S., Singh, R., & Kattimani, P. (2025). Thermal scrutinization of MHD Darcy–Forchheimer flow of hybrid nanofluid over a stretching sheet with Richardson number and quadratic thermal radiation: Hyperbolic tangent model. *Multiscale and Multidisciplinary Modeling, Experiments and Design*, 8(3), 171. doi: 10.1007/s41939-025-00745-y

[13] Takhar, H.S., Chamkha, A.J., & Nath, G. (1999). Unsteady flow and heat transfer on a semi-infinite flat plate with an aligned magnetic field. *International Journal of Engineering Science*, 37(13), 1723–1736. doi: 10.1016/S0020-7225(98)00144-X

[14] Takhar, H.S., Chamkha, A.J., & Nath, G. (2001). Unsteady three-dimensional MHD-boundary-layer flow due to the impulsive motion of a stretching surface. *Acta Mechanica*, 146(1), 59–71. doi: 10.1007/BF01178795

[15] Jagadha, S., Gopal, D., Patil, N., Singh, S., Kishan, N., & Abhilasha, S.K. (2025). Effect of higher order chemical reaction and

Joule heating on rotational and permeable radiative MHD flow of Casson manganese ferrite fluid with heat generation/absorption. *Multiscale and Multidisciplinary Modeling, Experiments and Design*, 8(3), 164. doi: 10.1007/s41939-025-00756-9

[16] Vinay Kumar, V., Sharma, R.P., & Naveen Kumar, R. (2025). The role of time-varying nanofluid flow and particle aggregation on the kinetics of homogeneous and heterogeneous reactions in position-controlled squeezing porous slider. *Proceedings of the Institution of Mechanical Engineers, Part N: Journal of Nanomaterials, Nanoengineering and Nanosystems*, 23977914251338162. doi: 10.1177/23977914251338162

[17] Banakar, V.R., Kumar, T., Ramachandran, T., Karthikeyan, A., & Karthik, K. (2025). Activity of Motile Microorganisms in Radiative Heat Transfer Analysis of Chemically Reactive Flow Between Stretching Upper and Rotating Lower Disks. *Heat Transfer*, 54(7), 4390–4406. doi: 10.1002/htj.70001

[18] Thumma, T., Mishra, S.R., Abbas, M.A., Bhatti, M.M., & Abdelsalam, S.I. (2022). Three-dimensional nanofluid stirring with non-uniform heat source/sink through an elongated sheet. *Applied Mathematics and Computation*, 421, 126927. doi: 10.1016/j.amc.2022.126927

[19] Banakar, V.R., Sollapur, S.B., Kedia, A., Singh, V., & Sarris, I.E. (2025). Levenberg–Marquardt artificial neural network approach to analyze tetra hybrid nanofluid flow over a rough rotating disk under low/high oscillating magnetic fields. *Modern Physics Letters B*. doi: 10.1142/S0217984925502641

[20] Algehyne, E.A., Alrihieli, H.F., Saeed, A., Dawar, A., & Kumam, P. (2022). Cattaneo–Christov heat flux theory toward the magnetohydrodynamic micropolar hybrid nanofluid flow past a stretching/shrinking sheet with non-uniform heat source/sink and thermal radiation. *ZAMM - Journal of Applied Mathematics and Mechanics / Zeitschrift Für Angewandte Mathematik Und Mechanik*, 102(10), e202200168. doi: 10.1002/zamm.202200168

[21] Salahuddin, T., Arshad, M., Siddique, N., Alqahtani, A.S., & Malik, M.Y. (2020). Thermophyical properties and internal energy change in Casson fluid flow along with activation energy. *Ain Shams Engineering Journal*, 11(4), 1355–1365. doi: 10.1016/j.asej.2020.02.011

[22] Hayat, T., Riaz, R., Aziz, A., & Alsaedi, A. (2020). Influence of Arrhenius activation energy in MHD flow of third grade nanofluid over a nonlinear stretching surface with convective heat and mass conditions. *Physica A: Statistical Mechanics and Its Applications*, 549, 124006. doi: 10.1016/j.physa.2019.124006

[23] Asjad, M.I., Zahid, M., Inc, M., Baleanu, D., & Almohsen, B. (2022). Impact of activation energy and MHD on Williamson fluid flow in the presence of bioconvection. *Alexandria Engineering Journal*, 61(11), 8715–8727. doi: 10.1016/j.aej.2022.02.013

[24] Samanta, A., & Mondal, H. (2023). Numerical simulation of bioconvectional nanofluidic flow in the presence of activation energy past a stretching cylinder subject to swimming micro-organisms. *Pramana*, 97(4), 182. doi: 10.1007/s12043-023-02644-8

[25] Srilatha, P., Karthik, K., Prasad, K.V., Abdulrahman, A., Kumar, R.S.V., Gowda, R.J.P., & Kumar, R.N. (2024). Dynamics of Fourier's and Fick's laws on the convectively heated oscillatory sheet under Arrhenius kinetics: The finite-difference technique. *Journal of Computational Science*, 82, 102428. doi: 10.1016/j.jocs.2024.102428

[26] Akbar, N.S., Nadeem, S., Ul Haq, R., & Khan, Z.H. (2013). Radiation effects on MHD stagnation point flow of nano fluid towards a stretching surface with convective boundary condition. *Chinese Journal of Aeronautics*, 26(6), 1389–1397. doi: 10.1016/j.cja.2013.10.008

[27] Malik, R., Khan, M., Munir, A., & Khan, W.A. (2014). Flow and Heat Transfer in Sisko Fluid with Convective Boundary Condition. *PLOS One*, 9(10), e107989. doi: 10.1371/journal.pone.0107989

[28] Shaw, S., Mahanta, G., & Sibanda, P. (2016). Non-linear thermal convection in a Casson fluid flow over a horizontal plate with convective boundary condition. *Alexandria Engineering Journal*, 55(2), 1295–1304. doi: 10.1016/j.aej.2016.04.020

[29] Wang, F., Ahmad, S., Al Mdallal, Q., Alammari, M., Khan, M.N., & Rehman, A. (2022). Natural bio-convective flow of Maxwell nanofluid over an exponentially stretching surface with slip effect and convective boundary condition. *Scientific Reports*, 12(1), 2220. doi: 10.1038/s41598-022-04948-y

[30] Abbas, M., & Khan, N. (2023). Numerical study for bioconvection in Marangoni convective flow of Cross nanofluid with convective boundary conditions. *Advances in Mechanical Engineering*, 15(11). doi: 10.1177/16878132231207625

[31] Rafiq, T., Mustafa, M., & Farooq, M.A. (2020). Modeling heat transfer in fluid flow near a decelerating rotating disk with variable fluid properties. *International Communications in Heat and Mass Transfer*, 116, 104673. doi: 10.1016/j.icheatmasstransfer.2020.104673

[32] Ahmad, L., Ahmed, J., & Ahmed, A. (2022). Thermal energy transport in thin film flow of nanofluid over a decelerating rotating disk. *Proceedings of the Institution of Mechanical Engineers, Part E: Journal of Process Mechanical Engineering*, 236(2), 491–499. doi: 10.1177/09544089211050717

[33] Ejaz, I., & Mustafa, M. (2022). A comparative study of different viscosity models for unsteady flow over a decelerating rotating disk with variable physical properties. *International Communications in Heat and Mass Transfer*, 135, 106155. doi: 10.1016/j.icheatmasstransfer.2022.106155

[34] Lin, Y., Cao, L., Tan, Z., & Tan, W. (2024). Magneto-hydrodynamics Marangoni boundary-layer copper/water nanofluid flow driven by surface temperature gradient over a rotating disk. *Physica Scripta*, 99(9), 095305. doi: 10.1088/1402-4896/ad6bcd

[35] Kamal, A.F.M., Faizan, M., & Zafar, S.S. (2024). Mixed convective magneto flow of nanofluid for the Sutterby fluid containing micro-sized selfpropelled microorganisms with chemical reaction: Keller box analysis. *Physica Scripta*, 99(9), 095202. doi: 10.1088/1402-4896/ad6642

[36] Rahman, M., Turkyilmazoglu, M., Bilal, M., & Sharif, F. (2023). On heat transfer with unsteady MHD nanofluid von Karman flow with uniform suction. *Pramana*, 97(4), 146. doi: 10.1007/s12043-023-02618-w

[37] Kattimani, P., Sollapur, S.B., Kedia, A., Singh, K., & Sarris, I.E. (2025). The Role of High-Oscillating Magnetic Field Dynamics in Nanofluid Flow. *Nano*, 2550101. doi: 10.1142/S1793292025501012

[38] Asma, M., Othman, W.A.M., Muhammad, T., Mallawi, F., & Wong, B.R. (2019). Numerical Study for Magnetohydrodynamic Flow of Nanofluid Due to a Rotating Disk with Binary Chemical Reaction and Arrhenius Activation Energy. *Symmetry*, 11(10), 1282. doi: 10.3390/sym11101282

[39] Mallikarjuna, A.N., Banakar, V.R., Abdulrahman, A., & Kumar, R.S.V. (2025). Study on thermophoretic deposition of particles and ratio of effective heat capacity: A collocation approach. *International Communications in Heat and Mass Transfer*, 169, 109841. doi:10.1016/j.icheatmasstransfer.2025.109841

[40] Jyothi, K., Sudarsana Reddy, P., & Suryanarayana Reddy, M. (2018). Influence of magnetic field and thermal radiation on convective flow of SWCNTs-water and MWCNTs-water nanofluid

between rotating stretchable disks with convective boundary conditions. *Powder Technology*, 331, 326–337. doi: 10.1016/j.powtec.2018.03.020

[41] Narayana, P.V.S., Akshit, S.M., Ghori, J.P., & Venkateswarlu, B. (2017). Thermal Radiation Effects on an Unsteady MHD Nanofluid Flow Over a Stretching Sheet with Non-Uniform Heat Source/Sink. *Journal of Nanofluids*, 6(5), 899–907. doi: 10.1166/jon.2017.1374

[42] Acharya, N. (2021). Spectral simulation to investigate the effects of nanoparticle diameter and nanolayer on the ferrofluid flow over a slippery rotating disk in the presence of low oscillating magnetic field. *Heat Transfer*, 50(6), 5951–5981. doi: 10.1002/htj.22157

[43] Varun Kumar, R.S., Kumar, R.N., Ben Ahmed, S., Madhu, J., Verma, A., & Punith Gowda, R.J. (2024). Unsteady flow of a ternary nanofluid over a slow-rotating disk subject to uniform suction and backpropagated neural network. *Numerical Heat Transfer, Part B: Fundamentals*, 85(12), 1705–1725. doi: 10.1080/10407790.2023.2269610

[44] Turkyilmazoglu, M. (2014). Nanofluid flow and heat transfer due to a rotating disk. *Computers and Fluids*, 94, 139–146. doi: 10.1016/j.compfluid.2014.02.009